



# Regolith-geology mapping with support vector machine: A case study over weathered Ni-bearing peridotites, New Caledonia



Florian De Boissieu<sup>a,\*</sup>, Brice Sevin<sup>b</sup>, Thomas Cudahy<sup>c</sup>, Morgan Mangeas<sup>a</sup>, Stéphane Chevrel<sup>d</sup>, Cindy Ong<sup>c</sup>, Andrew Rodger<sup>c</sup>, Pierre Maurizot<sup>b</sup>, Carsten Laukamp<sup>c</sup>, Ian Lau<sup>c</sup>, Touraivane Touraivane<sup>e</sup>, Dominique Cluzel<sup>e</sup>, Marc Despinoy<sup>a</sup>

<sup>a</sup> UMR ESAPCE-DEV, IRD, BPA5, 98848 Noumea, New Caledonia

<sup>b</sup> Geological Survey of New Caledonia, DIMENC, BP 465, 98845 Noumea, New Caledonia

<sup>c</sup> CSIRO Mineral Resources Flagship, CSIRO, 26 Dick Perry Avenue, Kensington, WA 6151, Australia

<sup>d</sup> BRGM, BP 6009, 45060 Orleans, France

<sup>e</sup> University of New Caledonia, BP R4, 98851 Noumea, New Caledonia

## ARTICLE INFO

### Keywords:

Hyperspectral  
Spectroscopy  
Recognition  
Classification  
Support vector machine  
Mineralogy  
Geology  
Iron oxide  
Serpentine  
Mapping

## ABSTRACT

Accurate maps of Earth's geology, especially its regolith, are required for managing the sustainable exploration and development of mineral resources. This paper shows how airborne imaging hyperspectral data collected over weathered peridotite rocks in vegetated, mountainous terrane in New Caledonia were processed using a combination of methods to generate a regolith-geology map that could be used for more efficiently targeting Ni exploration. The image processing combined two usual methods, which are spectral feature extraction and support vector machine (SVM). This rationale being the spectral features extraction can rapidly reduce data complexity by both targeting only the diagnostic mineral absorptions and masking those pixels complicated by vegetation, cloud and deep shade. SVM is a supervised classification method able to generate an optimal non-linear classifier with these features that generalises well even with limited training data. Key minerals targeted are serpentine, which is considered as an indicator for hydrolysed peridotitic rock, and iron oxy-hydroxides (hematite and goethite), which are considered as diagnostic of laterite development. The final classified regolith map was assessed against interpreted regolith field sites, which yielded approximately 70% similarity for all unit types, as well as against a regolith-geology map interpreted using traditional datasets (not hyperspectral imagery). Importantly, the hyperspectral derived mineral map provided much greater detail enabling a more precise understanding of the regolith-geological architecture where there are exposed soils and rocks.

## 1. Introduction

The last 20 years has seen the emergence of proximal and remote multispectral and hyperspectral sensing technologies, which have opened up new opportunities in natural resource mapping and monitoring. In contrast to multispectral systems like the satellite ASTER system (Abrams et al., 2015) that measure 3–30 spectral bands, hyperspectral sensors measure up to hundreds of spectral bands. Most hyperspectral sensors measure across the visible, near infrared and shortwave infrared (VNIR-SWIR; 400–2500 nm), and to a lesser degree, thermal infrared (TIR 7600–14,000 nm) wavelengths regions. Importantly, many major rock types and their alteration products (metamorphic, metasomatic and weathering) comprise diagnostic absorption features at these wavelengths (Clark and Roush, 1984; Lyon, 1965; Lyon and Burns, 1963). Hyperspectral systems are now operating using

drill core (Cudahy et al., 2009; Huntington et al., 2005), in the field (Sonntag et al., 2012) and from airborne (Cocks et al., 1998; Crowley et al., 1989; Green et al., 1998; Kruse et al., 2006; Rowan et al., 2004; van der Meer et al., 2012) and spaceborne (Cudahy et al., 2001; Kruse et al., 2003) platforms.

The transformation of raw hyperspectral data into mineral products of value for a given application usually involves a series of image processing steps, including: (i) calibration of instrument data to radiance at sensor; (ii) radiative transfer correction; and (iii) information extraction. The last step has many possible approaches from unmixing strategies (Boardman et al., 1995) to spectral feature extraction (Sunshine et al., 1990) and various classification methods (Sabins, 1999; Vapnik, 1998). Two of the largest, publicly accessible airborne hyperspectral mineral mapping surveys (~250 flight lines) completed to date, namely Afghanistan (King et al., 2011) and north-Queensland

\* Corresponding author.

E-mail address: [florian.de-boissieu@teledetection.fr](mailto:florian.de-boissieu@teledetection.fr) (F. De Boissieu).

in Australia (Cudahy et al., 2008), generated mineral maps using unmixing and spectral feature extraction methods, respectively. However, these maps are formed of a suite of mineral product layers requiring an end user able to interpret them into valuable geological information appropriate for their needs.

One way to bridge the gap between “mineral information” and “geological knowledge” is to use a classification method applied to the suite of mineral maps instead of raw reflectance or radiance data, as often is the case. For this task, a promising method able to work with complex associations and relatively few training data is support vector machine (SVM) (Camps-Valls and Bruzzone, 2005). SVM is a kernel-based method able to process efficiently non-linearly separated classes, which is common in natural systems, though few studies have applied it to geological applications (Abedi et al., 2012; Kavitha and Arivazhagan, 2010).

New Caledonia is economically reliant on its lateritic Ni production so that new discoveries, sourced in areas that are relatively poorly mapped (Mudd and Jowitt, 2014), will be required in the future to improve resource management. This article evaluates the combined use of mineral spectral feature extraction and SVM classification on the first airborne hyperspectral imagery collected over New Caledonia. The aim is to create a regolith-geology thematic map targeting Ni mineralisation associated with weathered peridotite. Potential complications include variable vegetative and cloud cover, terrain effects (including illumination-shadowing) and surface mineralogy unrelated to the geological target. To reduce complexity, spectral features based on within-pixel normalisation were designed to measure key minerals, such as serpentine (target bedrock) and iron oxides (laterite cover). The results are validated and interpolated into the sub-surface with field sample data, digital elevation model and a conventional regolith map.

## 2. Location and geology

The study area in New Caledonia (Fig. 1) is mountainous and variably covered by vegetation developed upon weathered peridotite. Peridotite is a coarse-grained mantle rock mostly composed of olivine and pyroxene (e.g. elements Si, Fe and Mg), which may be partially altered into hydrous Mg silicate (serpentine). During near-surface weathering (Nahon, 2003), percolating waters leach mobile elements Mg and Si to leave a lateritic residue of  $\text{Fe}^{3+}$  and Ni. Ni can be concentrated into hydrous Ni-Mg silicates collectively referred to as “garnierite” and iron oxyhydroxides (goethite and hematite) (Fig. 2).

In the study area the peridotite bedrock is covered by a lateritic weathering profile composed from the base to the top of coarse saprolite (partially weathered rock), yellow laterite (goethite), red laterite

(mixed goethite and hematite), ferricrete (hardened hematite) and a discontinuous pisolith layer (hematite) (Fig. 2).

From a Ni exploration perspective, the most prospective areas for surface sampling are saprolite and yellow laterite (Fig. 2). Thus generating maps from the remote sensing data that show development of these units would be valuable for follow-up field exploration programs. Areas of in situ ferricrete and red laterite are also potentially prospective because they may be underlain by thick layers of Ni-bearing laterite and saprolite.

Given the above, the target minerals with diagnostic hyperspectral absorption features at VNIR-SWIR wavelengths include iron oxides (hematite and goethite) and serpentine (van der Meer, 1995). Olivine, clinopyroxene and orthopyroxene, do not have diagnostic features at VNIR-SWIR wavelength, but could be measureable at TIR wavelengths (Launer, 1952; Logan et al., 1973; Lyon, 1965; Lyon and Burns, 1963; Salisbury and Walter, 1989), unfortunately not available for this survey.

## 3. Material and methods

### 3.1. Data

A range of data was acquired for this study, namely: (i) airborne hyperspectral HyMap™ imagery; (ii) field hyperspectral data; (iii) ground geological information; and (iv) a regolith map interpreted from other spatial data.

#### 3.1.1. Airborne HyMap imagery

The HyMap system (Cocks et al., 1998) was used to collect airborne hyperspectral imagery. HyMap is a whiskbroom imaging sensor that measures 126 bands over the wavelength range of 450–2500 nm across a 512 pixel swath. Twenty-five HyMap flight-lines at approximately 3.6 m pixel resolution from seven test sites across New Caledonia covering a total area of about 500 km<sup>2</sup> (Fig. 1) were acquired in 2010. This study focuses on a single, cloud-free flight-line (3 × 15 km area) from the Fantoche plateau near Tiebaghi (Fig. 1) where soils and geology are exposed through variable vegetation cover. Data were supplied as both radiance at sensor and surface reflectance, together with geolocation and other survey information.

#### 3.1.2. Field sample spectra

Field samples were measured using an Analytical Spectral Device (ASD) FieldSpec 3 spectrometer, which senses 2150 wavelengths between 350 and 2500 nm, i.e. with 1 nm resolution. Each field measurement was taken under sun illumination at a distance of 1 m from

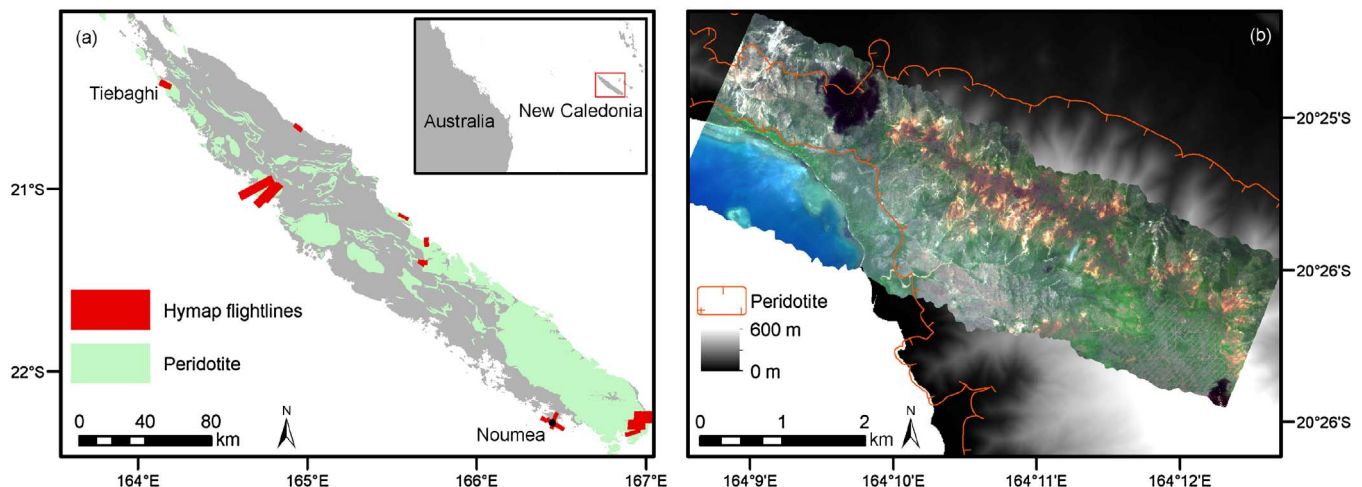


Fig. 1. (a) New Caledonia main island, with the 2010 HyMap survey coverage. (b) HyMap natural color image of the Tiebaghi study area. Exposed regolith of the Fantoche plateau (at the summit of Teibaghi massif) is apparent as dark white-red-brown tones.

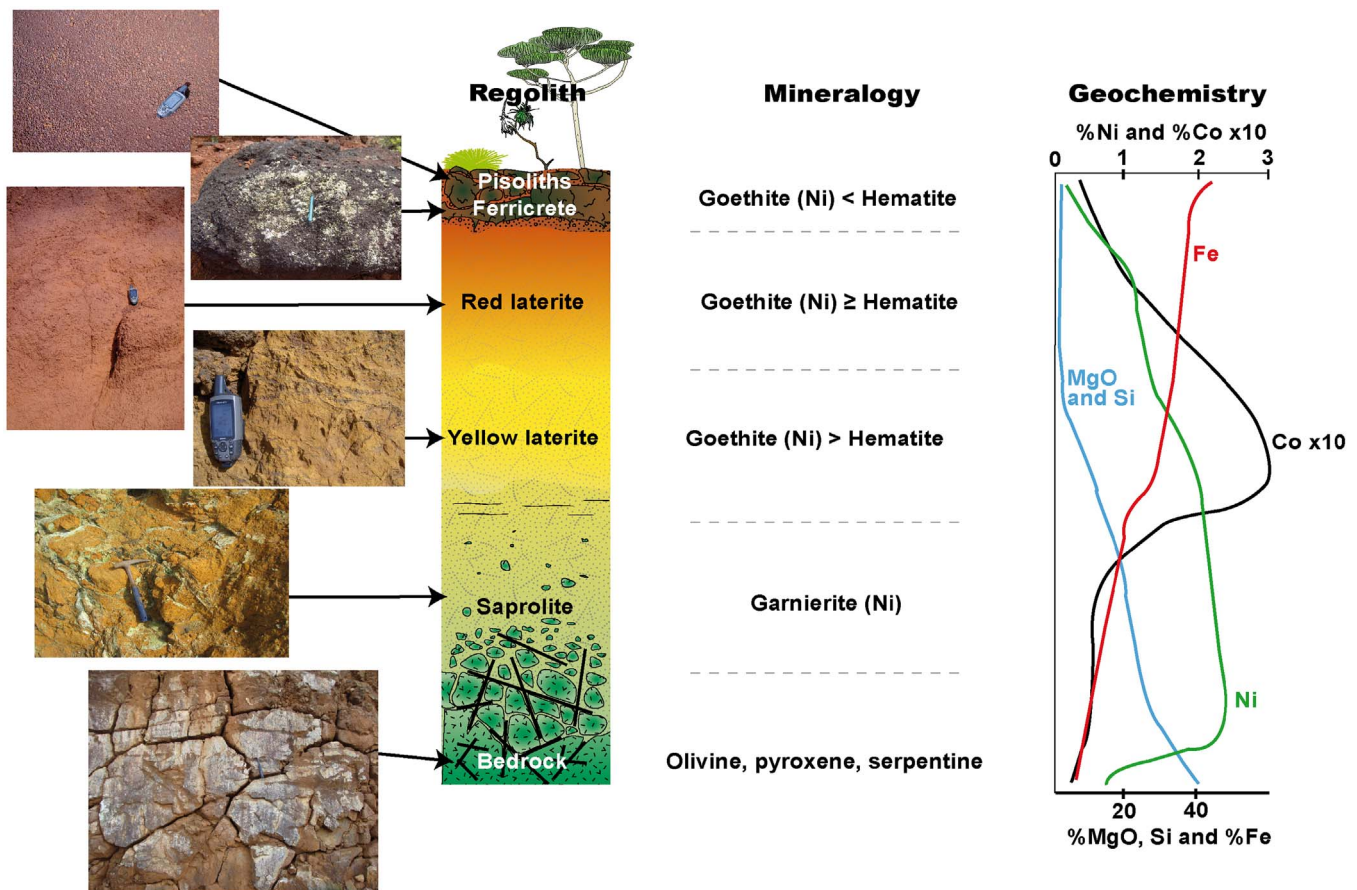


Fig. 2. Schematic lateritic weathering profile, including selected field photographs, geochemistry and mineralogical information (Sevin, 2014).

the target (data removed in the 1400 and 1900 nm water vapour absorption regions) and/or under artificial lighting (halogen at night) at contact measurement. A Spectralon™ panel was used as the reflectance reference standard. A total of 212 reflectance spectra comprising 146 sun-illuminated and 48 contact spectra were collected from soil, weathered rock and vegetation samples of the four main test sites of geological interest.

### 3.1.3. Interpreted regolith mapping

A geologist (B. Sevin (Sevin, 2014)) provided regolith categorization at massif scale (Fig. 3, plain colors), metric scale (Fig. 3, hatched colors) and sub-metric scales (field samples), with different classification schemes depending on the observation scale.

At metric and sub-metric scales, the classification was based on field interpretation of spatial context, color and sample texture and allowed a categorization using the scheme shown in Fig. 2. For example, ferricrete is recognized as being indurated and hematite-rich (dark red to even black color) whereas saprolite is light green with preserved rock/mineral textures. Field sites of bare soil with homogeneous regolith type and sufficient size to be visible on HyMap imagery, were precisely delimited with GPS on the field (Fig. 3, hatched colors). Table 1 gives the spatial cover of the field sites coincident with the HyMap imagery.

The regolith-geology map at the massif scale (Fig. 3, plain colors) was generated independently from this study. It was based on field interpretation combined with other information at a broader scale (1:25000) (e.g. digital elevation model for the geomorphology and orthophotos for the color of the regolith units) and with a coarser mining classification scheme. For this map, a morphology criterion into either “thick” laterite (usually grouping red to yellow laterite) or “thin” laterites (usually grouping yellow laterite to saprolite) is preferred to the color criterion that can be tricky considering the distance of observation

and the vegetation cover.

One can notice on Fig. 3 that some field sites are covering different regolith types illustrating the difficulty to map accurately the regolith from field interpretation. The field sites are considered as “truth” in this study for both the SVM training and validating the airborne hyperspectral processing and derived products.

## 3.2. Image processing

Image processing of the HyMap data (Fig. 4) involved a sequence of steps, including: (i) pre-processing to generate geolocated surface reflectance; (ii) spectral feature extraction; and (iii) SVM classification.

### 3.2.1. Pre-processing

The HyMap airborne hyperspectral data were delivered as radiance at sensor ( $\text{W sr}^{-1} \text{m}^{-2} \mu\text{m}^{-1}$ ), which were then converted to bi-directional, surface reflectance using a MODTRAN 5 (Berk et al., 2006) based method called SODA (Rodger, 2011). SODA provides a more accurate estimate of atmospheric column water vapour (ACWV) for each pixel as well as a means for identifying and correcting for any unexpected instrument wavelength calibration issues. For the New Caledonian dataset, the water vapour feature centred at 1130 nm appeared to over-influence the ACWV estimation, such that the 940 nm feature was used instead.

The HyMap data were geocorrected by HyVista™ proprietary software using the sensor position acquired during flight and the NASA SRTM topographic map with 90 m spatial resolution (<http://www2.jpl.nasa.gov/srtm>). This geocorrection was further improved using a 3rd order polynomial fit on 36 ground control points, leading to a mean error of 7.8 m.

Finally, to generate airborne spectra comparable with associated



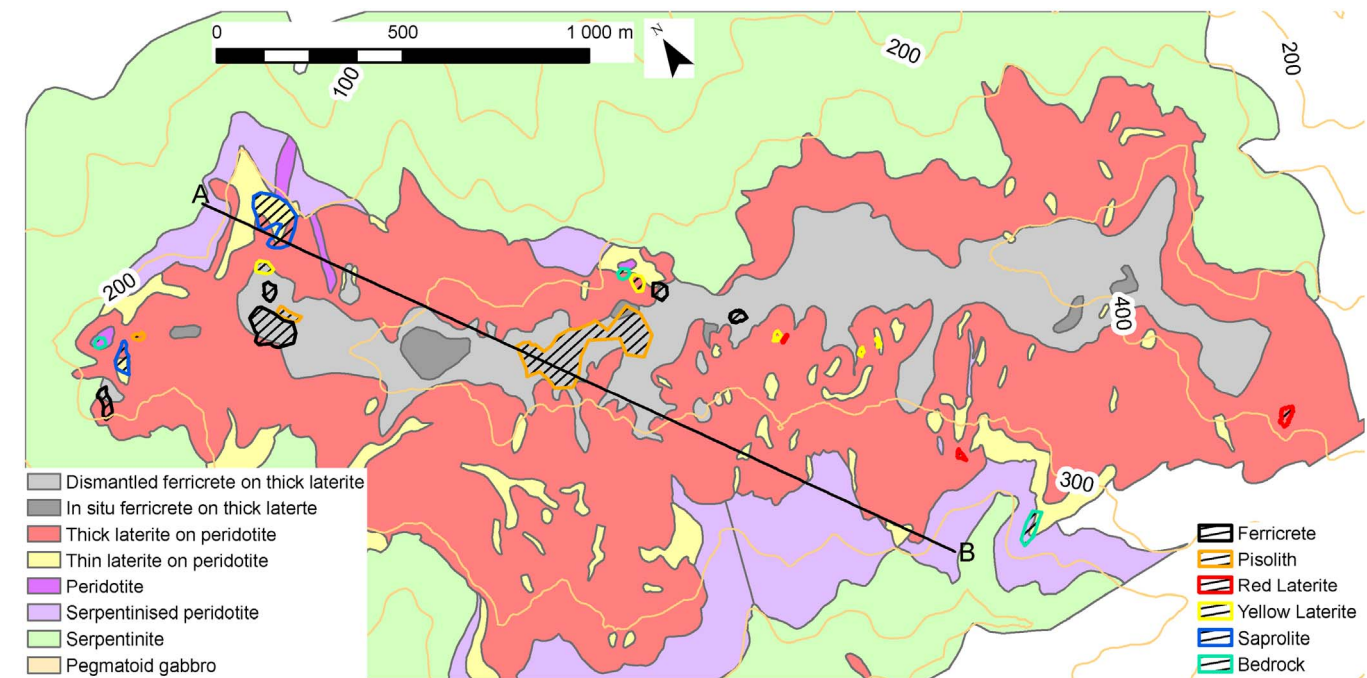


Fig. 3. Surface regolith-geology map of the Fantoche plateau (massif of Tiebaghi) interpreted from traditional exploration and geo-spatial data. In plain color, the massif scale map. In hatched color, homogeneous field sites selected from field interpretation at metric scale. A, B line is used in Fig. 9.

Table 1  
Number of pixels for each regolith-geology class.

	Ferricrete	Pisolith	Red Lat.	Yellow Lat.	Saprolite	Bedrock
Surface (m <sup>2</sup> )	2424	23937	661	2968	7089	1115
Surface (pix.)	187	1847	51	229	547	86

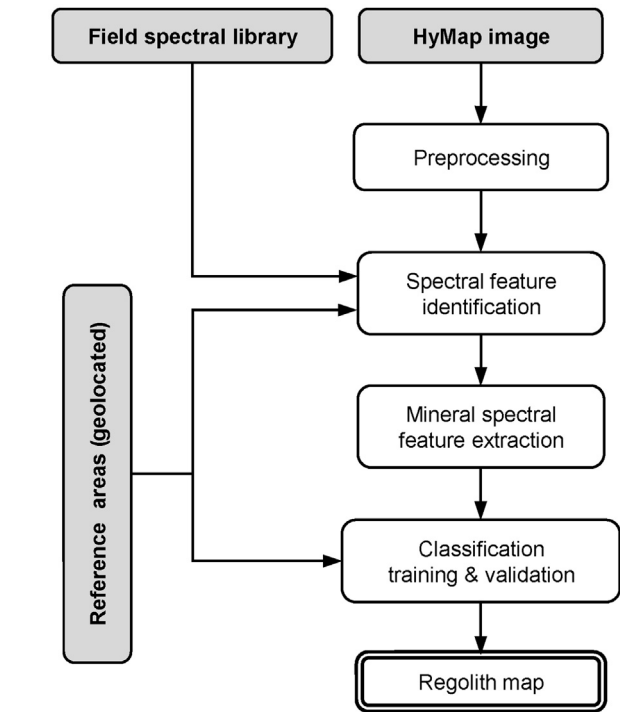


Fig. 4. Diagram of the processing steps to produce the mineral and regolith maps.

field sample spectra, the HyMap apparent reflectance spectra were normalized to their pixel spectral-mean, which removes the pixel-

specific albedo (Cudahy et al., 2008) and the complication of topographic illumination-shading effects.

### 3.2.2. Spectral feature extraction

Reflectance spectra are often processed to remove the broad continuum response to leave as residual any narrow absorption features (Clark and Roush, 1984). This operation removes complications associated with the effect of a sloping continuum on the wavelength of given absorption feature (van der Meer, 2000). The magnitude of absorption (relative to the continuum) of a given mineral absorption can be used as an indicator for the abundance of that mineral, whereas its wavelength is related to its composition (Clark and Roush, 1984; Kokaly and Clark, 1999). As an example, goethite and hematite have major crystal field electronic absorptions located around 865 nm and 930 nm, respectively. Thus, the maximum absorption wavelength around 900 nm may be used as an indicator of hematite/goethite ratio. Iron oxides also have a major charge transfer absorption around 900 nm. Therefore, the depth of absorption around 900 nm is also significant of the abundance of iron oxides. However, absolute concentration and composition are often not straight-forward and dependant of the geological environment due to non-linear changes of transparency with wavelength, optical depth, scattering and other possible overlapping mineral absorptions.

In this study, the depth and the wavelength position of selected mineral absorption features were gauged using a two-step operation, namely: (i) continuum removal; and (ii) absorption parameterisation. The wavelength position and the depth of maximum of absorption are determined for each key mineral from  $A(\lambda)$  calculated using Eq. (1) (Kokaly and Clark, 1999), where  $\hat{CR}(\lambda)$  is the continuum removed spectrum modelled using a 4th order polynomial fitted between two endpoints that span the edges of the target absorption.

$$A(\lambda) = 1 - \hat{CR}(\lambda) \quad (1)$$

A list of these feature parameters is provided in Table 2.

In addition to these mineral spectral features, the HyMap data were masked to remove all pixels dominated by occulting effects, such as vegetation, cloud, deep shadow or water. The vegetation mask is based

**Table 2**  
HyMap spectral features and their interpreted mineral information.

Spectral features	D <sub>660</sub>	D <sub>900</sub>	W <sub>900</sub>	D <sub>2120</sub>	D <sub>2310</sub>
Mineral characteristics	Goethite & garnierite abundance	Iron oxyhydroxide abundance	Goethite/Hematite abundance ratio	Serpentine abundance	Serpentine abundance

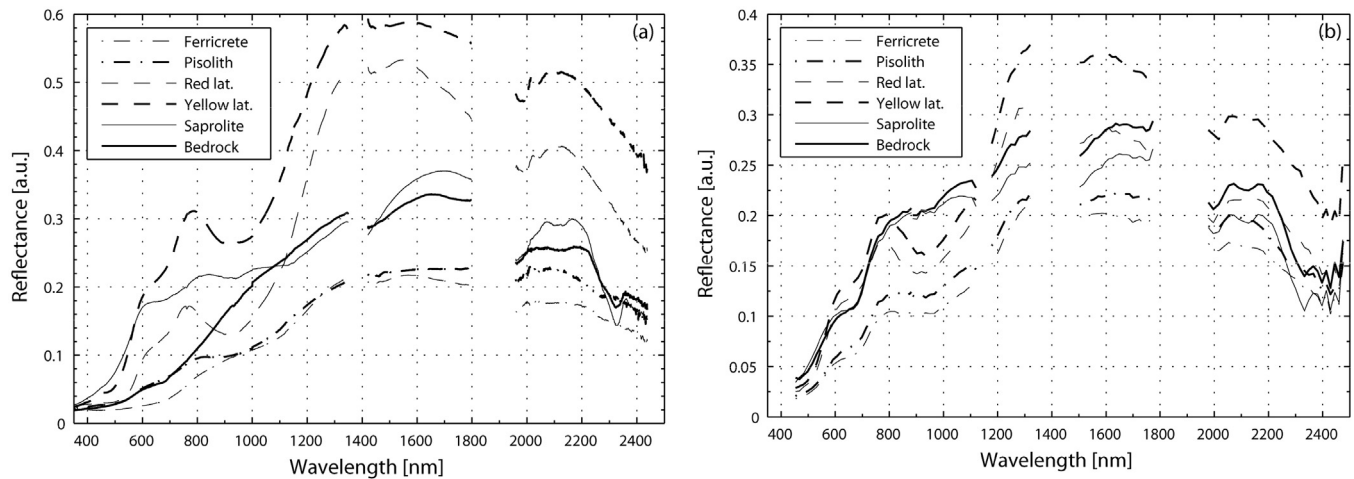


**Fig. 5.** Regolith-geology VNIR-SWIR reflectance spectra measured with: (a) ASD spectrometer on the field under sunlight, (b) airborne HyMap. Although the global magnitude and the contrast are higher for field spectra than for HyMap spectra, the absorptions are occurring at the same wavelengths for the same classes.

on a Normalized Difference Vegetation Index (NDVI), calculated using Eq. (2) where  $\rho_{680}$  and  $\rho_{760}$  are the reflectance at wavelength 680 nm and 760 nm.

$$NDVI = \frac{(\rho_{760} - \rho_{680})}{(\rho_{760} + \rho_{680})} \quad (2)$$

An NDVI mask value  $> 0.25$  was selected as the threshold for culling those pixels with too much green vegetation cover. Similarly, deep shadow and water are masked using the reflectance at 1650 nm ( $\rho_{1650}$ ) where  $\rho_{1650} > 0.08$ . However, this mask also removed regolith surfaces with low albedo, such as ferrous and/or manganese bearing oxyhydroxides.

### 3.2.3. Support vector machine

The support vector machine classification method is based on the idea of defining the optimal boundary between two classes with the training samples closest to the boundary, called the support vectors. For a linear binary classification problem, the optimal separating hyperplane is the one minimizing the error of classification but maximizing the distance (or margin) between the vectors closest to the hyperplane and the hyperplane. The kernel trick extends this method to non-linear separation problems, using a kernel function instead of the dot product to measure the similarity between vectors. And for the case of non separable classes, a hinge loss function is added with a regularization user-defined parameter  $C$  that tunes a compromise between the acceptable amount of error and the size of the margin. Importantly, compared to other classification algorithms (e.g. Neural Networks), the SVM can work with small training datasets such as in this study with classes having less than 50 samples.

$$K(\mathbf{x}_i, \mathbf{x}_j) = e^{-\gamma \|\mathbf{x}_i - \mathbf{x}_j\|_2^2} \quad (3)$$

The kernel function used in this experiment is a Gaussian radial basis function defined by Eq. (3) for two input vectors  $\mathbf{x}_i$  and  $\mathbf{x}_j$ , with user-defined  $\gamma$  parameter. As the labelled datasets were too small to tune  $C$  and  $\gamma$ , they were set respectively to 1 and  $1/d_x$  with  $d_x$  the input dimension. The SVMs were computed with R language using *e1071* library, the R implementation of LIBSVM (Chang and Lin, 2011).

The extension of the SVM classifier to the multi-class problem is

made with a pair-wise classification. Followed by a voting strategy (Fauvel et al., 2006). For more details on the SVM algorithm, one can refer to Chang and Lin (2011).

The classes are considered to have an equi-probability of appearance as we have no *a priori* information at that stage. Therefore, an equi-distributed training dataset between classes is built up with 40 pixels/class randomly selected from the labelled pixels mentioned in Section 3. A 10-fold cross-validation procedure is applied on the training dataset, giving training and validation accuracies to evaluate the performance of the classifier. The remaining pixels of the labelled dataset are classified, giving the test accuracy, to evaluate the generalization of the classifier. The classifier is evaluated at the class level with the confusion matrix counting the confusions between labels and classification results. As the labelled dataset is unevenly distributed between classes, the experiment is repeated 10 times (each training datasets randomly selected among labelled data) over which the accuracies are averaged.

## 4. Results

### 4.1. Airborne and field spectra

Representative field ASD and HyMap pixel spectra of different regolith types are provided in Fig. 5a and b, respectively. Importantly, there is a high degree of similarity between the field and airborne reflectance spectra, indicating the effectiveness of the HyMap pre-processing. Readily evident are absorptions at 400, 660 and 900 nm related to iron oxides (Cudahy and Ramanaidou, 1997). These are most pronounced in the red and yellow laterite spectra but are weakly developed in the less weathered bedrock and saprolite samples/pixels. The lower overall reflectance (albedo) for both the ferricrete and the pisolith can be possibly caused by either the reduction of some of the iron contained in the related oxyhydroxides by fires (Anand and Paine, 2002; Cudahy and Ramanaidou, 1997) or the development of manganese-bearing minerals. Importantly, this opaque spectral behaviour can suppress the continuum- depth of the ferric oxide absorption at 900 nm, making samples/pixels rich in iron oxide to have an apparently lower abundance, such as the pisolith and ferricrete spectra in Fig. 5. Absorptions



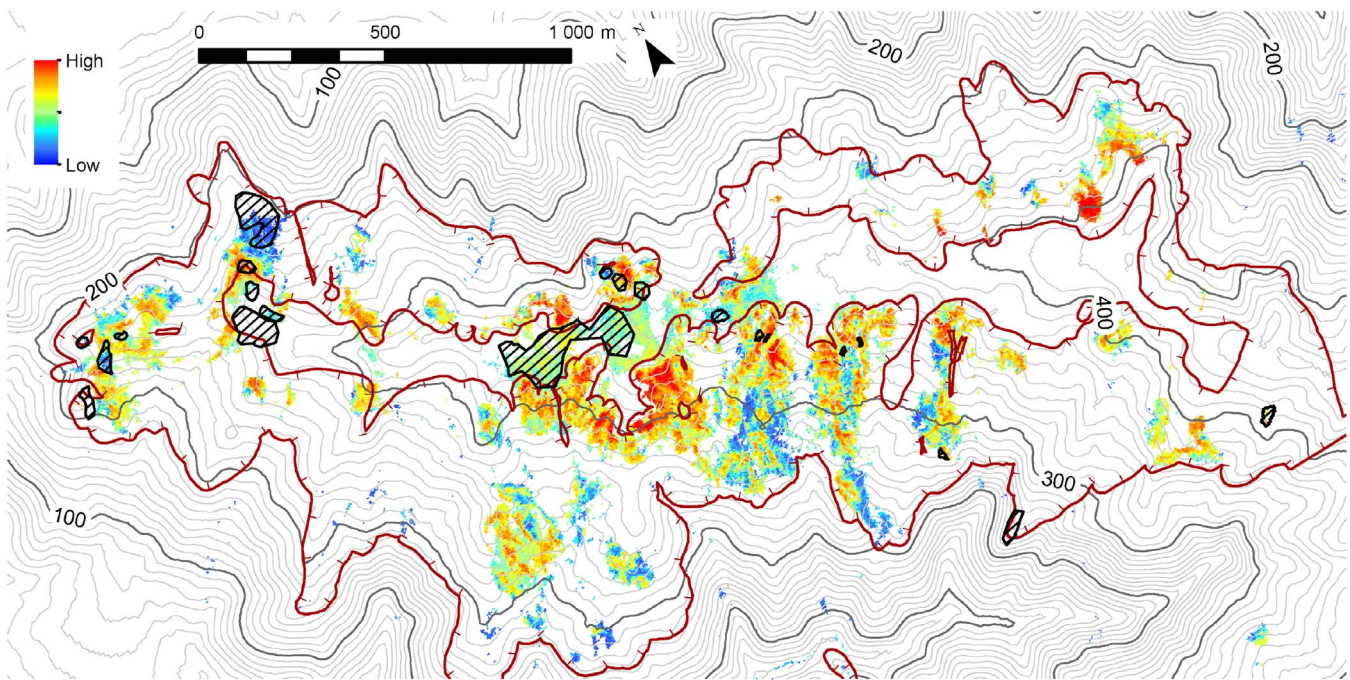


Fig. 6. HyMap  $D_{900}$  absorption feature map designed to map the abundance of iron oxyhydroxides. The interpreted laterite boundary (red solid line) and the field sites (hatched areas) from Fig. 3 are annotated. (For interpretation of the references to color in this figure legend, the reader is referred to the web version of this article.)

at 2120 and 2310 nm are considered diagnostic of serpentine (van der Meer, 1995); however similar absorptions also characterise dry plant material, causing potential problems in accurate identification and mapping.

Five mineral-spectral features were extracted from the field and airborne spectra, namely: the continuum-removed depth of the maximum of absorption at 660, 900, 2120 and 2310 nm ( $D_{660}$ ,  $D_{900}$ ,  $D_{2120}$ ,  $D_{2310}$ ); and the wavelength position of the absorption maximum around 900 nm ( $W_{900}$ ). Table 2 summarises these spectral features and their targeted mineral information.

#### 4.2. Spectral parameter mineral maps

Two of the five spectral feature mineral maps are presented here, namely:  $D_{900}$  which targets the iron oxyhydroxide mineral abundance (Fig. 6); and  $D_{2310}$  which targets the serpentine abundance (Fig. 7). An important part of the study area is masked due to dense vegetation, in particular for the regions interpreted as serpentinised peridotite and serpentinite (Fig. 3). The vegetation free areas are corresponding mostly to the upper sides of the plateau interpreted as thin and thick laterite (Fig. 3).

The  $D_{900}$  map (Fig. 6) shows similarity with the interpreted distribution of thick and thin laterite (Fig. 3) where high iron oxide abundance is detected, with increasing abundance approaching the contact with the overlying ferricrete. As expected, the abundance of iron oxide drops on the field sites identified as saprolite and bedrock (blue and cyan hatched areas Fig. 3). As noted for the field and HyMap spectra (Fig. 5), the ferricrete is as well associated with a lower intensity of  $D_{900}$  presumably because of the effect of complicating opaque phase.

The  $D_{2310}$  map (Fig. 7) shows a spatial distribution opposite to  $D_{900}$  map, with higher serpentine abundance over the field sites interpreted as saprolite and bedrock (blue and cyan hatched areas Fig. 3). Comparing to the regolith-geology map (Fig. 3), areas of well developed  $D_{2310}$  serpentine absorption (dotted polygons Fig. 7) are located over thick or thin laterite, including up to the contact with the overlying ferricrete. Interestingly, this  $D_{2310}$  serpentine absorption generally occurs in patches, separated by large areas of laterite with no apparent

serpentine (blue areas in Fig. 7), which is indicating localised erosion and/or hydrolysis reactions during serpentinisation such as along fluid pathways. However, this pattern differs from the interpreted geology (Fig. 3) which instead shows a large, flat tabular serpentinised peridotite directly below the laterite blanket. This difference can be explained by the difficulty of conventional regolith-geology methods to accurately map the distribution of a specific mineral like serpentine.

#### 4.3. SVM regolith mapping

The results for the SVM classification modelling into six regolith units using the five input spectral features (Table 2) are provided in Fig. 8. This modelled map shows broad similarity with the interpreted regolith-geology (Fig. 3) though in detail there are differences, similarly to those observed in the spectral feature maps (Figs. 6 and 7). For example, modelled red and yellow laterite generally equate to interpreted areas of thick and thin laterite in Fig. 3. However, similar to  $D_{2310}$  serpentine absorption map, there are patches of modelled saprolite (blue color in Fig. 8) within laterite of the interpreted map.

Ferricrete and pisolith patterns are located at the top of the lateritic profile, especially along higher parts of the topography, and match interpreted regolith-geology map (Fig. 3) even though no particular feature was used for the low spectral albedo characteristic of these classes.

The effect of terrain and erosion of the original blanket of laterite is apparent in the cross-section (A, B in Figs. 3 and 9) generated from a high resolution digital elevation model (DEM) and the spectral feature plus SVM classification map (Fig. 8). That is, interpolation from the surface measurements into the subsurface assuming a flat-lying, “layer-cake” model yields regolith architecture consistent with the dissected lateritic terrain. For example, in the central area of high ground (C in Fig. 9) there exists the thickest (~30 m) and most complete preservation of the laterite profile from bedrock to ferricrete. Elsewhere, either this profile is eroded down to saprolite and/or bedrock (e.g. D in Fig. 9) or the lateritic profile is much thinner (e.g. E in Fig. 9).



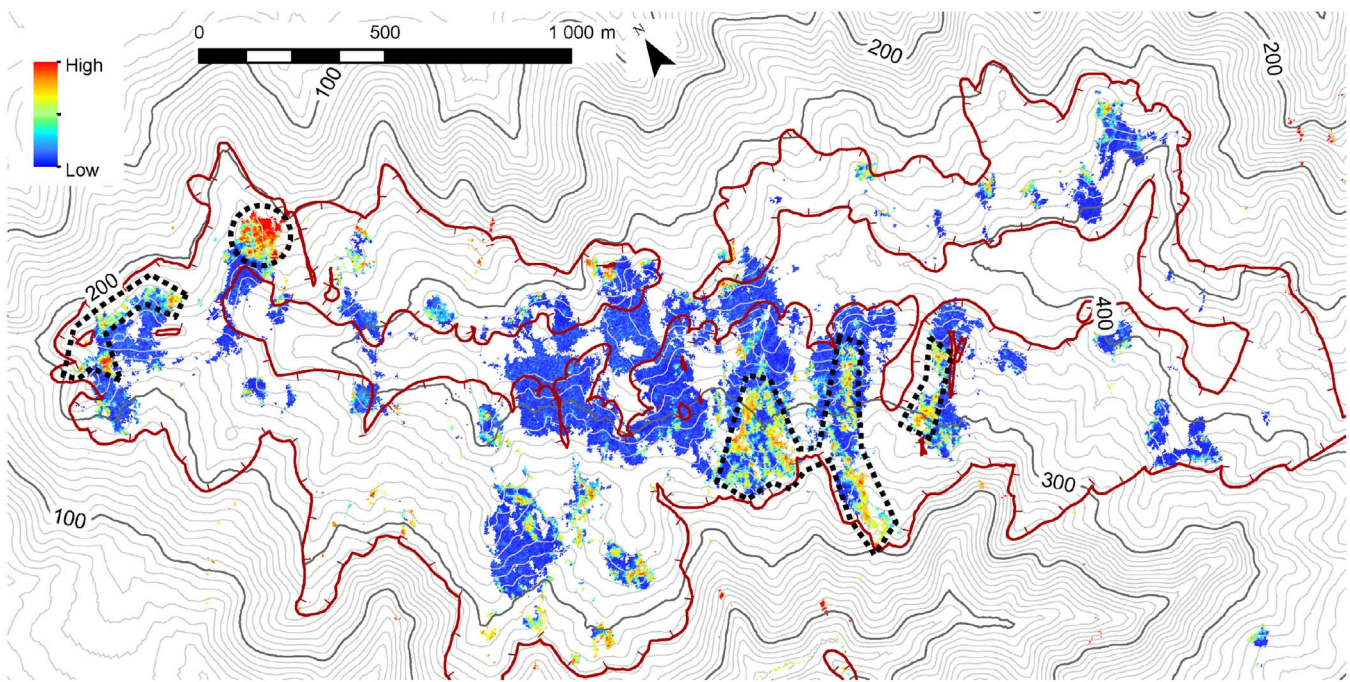


Fig. 7. HyMap D<sub>2310</sub> absorption feature map designed to map the abundance of serpentine. Areas rich in serpentine (dotted black line = low values for  $D_{900}$ , i.e. low iron oxide content in Fig. 6) and interpreted laterite boundary (red solid line) are annotated. (For interpretation of the references to color in this figure legend, the reader is referred to the web version of this article.)

#### 4.4. Accuracy assessment

To enable an estimate of the accuracy of the regolith-geology SVM classification, it was assumed that truth is the geologist interpreted regolith-geology of the field sites (hatched areas of Fig. 3) that were determined specifically for this study. The accuracy assessment results (Table 3) show an overall performance of > 70% classified correctly. The scores are similar for training, validation and test datasets, which attests a negligible overtraining. The confusion matrix (Table 4) shows best results for ferricrete, yellow laterite and bedrock (77%–83%). The

poorest results are obtained for pisolith, red laterite and saprolite (67%–69%). However these classes are mainly confused with ferricrete, yellow laterite and saprolite respectively. These particular errors make sense geologically because the associations share similar mineralogy. For example, serpentine can be developed in both bedrock and saprolite, similarly, iron oxide in both yellow and red laterite.

#### 5. Discussion and conclusions

This study shows that an accurate map of the regolith-geology can

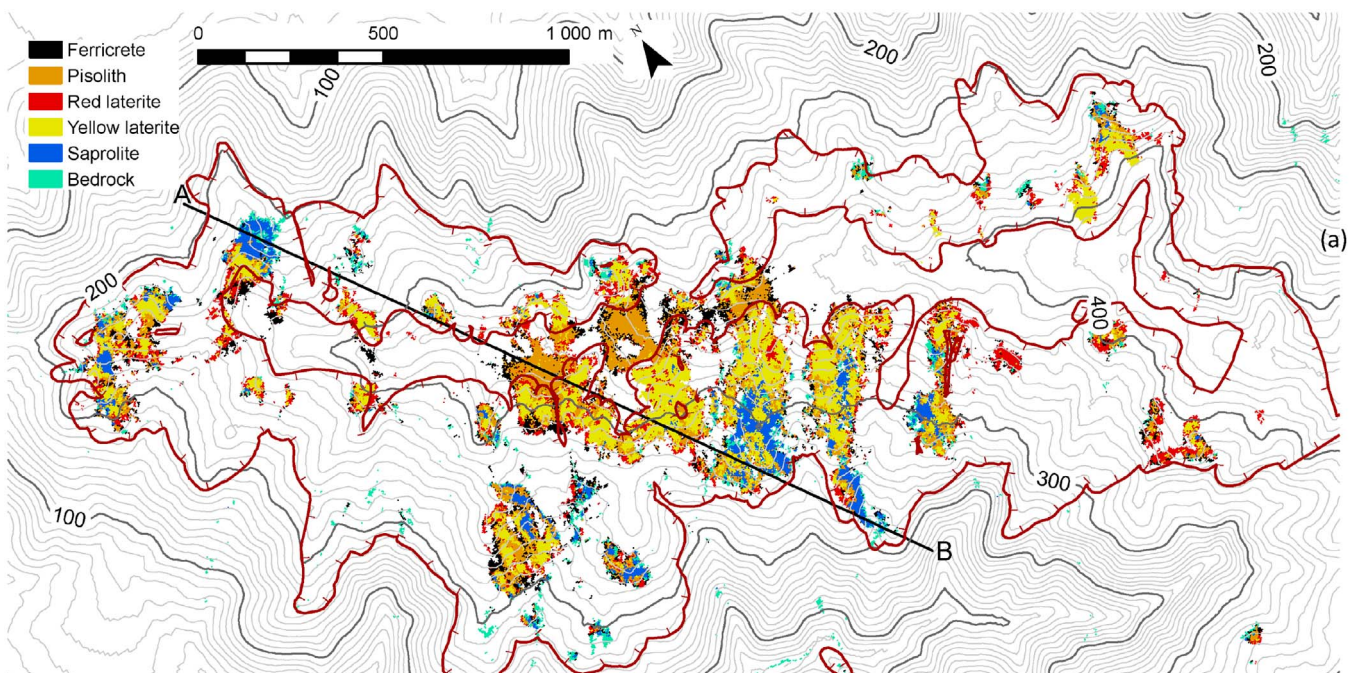


Fig. 8. Modelled regolith-geology map generated using SVM and five input spectral features (Table 2). The cross section A, B and interpreted laterite boundary (red line) are annotated. (For interpretation of the references to color in this figure legend, the reader is referred to the web version of this article.)



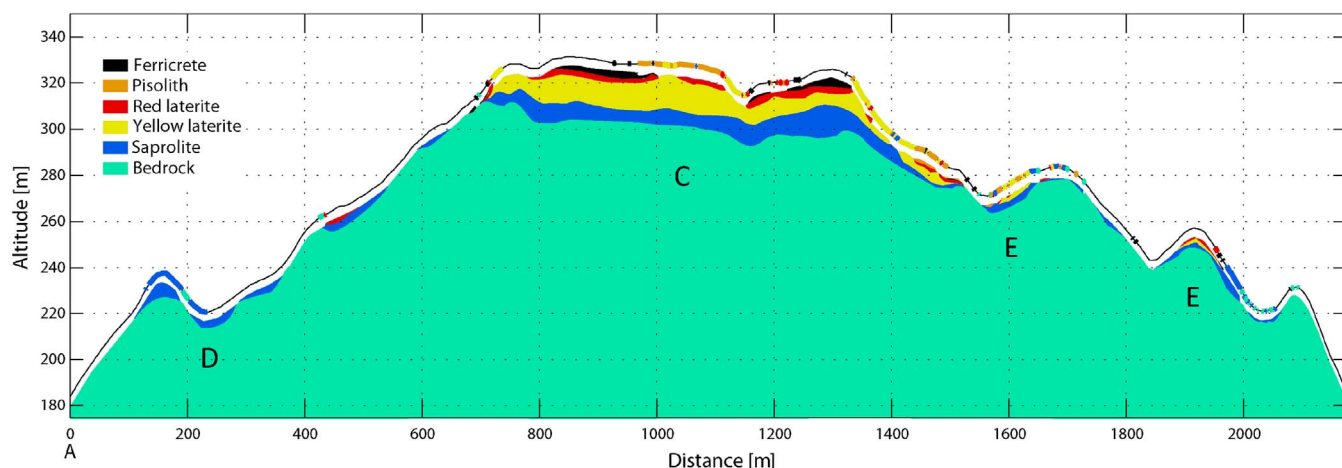


Fig. 9. Cross section A, B (Figs. 3 and 8) showing the resultant regolith-geology constructed using the modelled surface regolith-geology (Fig. 8) and a 10 m resolution digital elevation model. The cross-section line has exaggerated vertical relief (5:1). Characters C–E point out the remnant layers after variable erosion along the crests.

Table 3

Apparent accuracies of the HyMap spectral feature plus SVM classification assuming that the interpreted regolith-geology map is “truth” (Fig. 3).

	Training	Validation	Test average	Test weighted ave.
Accuracies [%]	78%	74%	76%	71%

Table 4

Confusion matrix for the HyMap data regolith-geology classification. Columns are geologist interpreted regolith-geology units (hatched, Fig. 3), rows are the SVM classification results. Results are given in percentage of class pixels (400 pixels/class).

	Ferricrete	Pisolith	Red lat.	Yellow lat.	Saprolite	Bedrock
Ferricrete	77.00	22.50	6.75	0.75	0.75	5.00
Pisolith	18.25	68.75	9.00	4.75	2.25	3.25
Red lat.	4.00	3.75	67.50	11.00	0.00	3.00
Yellow lat.	0.50	4.75	14.25	77.25	4.25	0.75
Saprolite	0.00	0.25	0.00	4.25	68.75	4.75
Bedrock	0.25	0.00	2.50	2.00	24.00	83.25

be generated from airborne hyperspectral imagery using a combination of spectral features and SVM methods. Whether this methodology is more efficient and accurate compared with others is not yet clear. Thus future studies could compare the current results for generating a regolith-geology map with: (i) SVM applied to the original reflectance data; (ii) SVM versus other classification methods using the spectral features as input. The importance of using a digital elevation model (DEM) in generating the 3D architecture of the regolith-geology is also critical, as shown in Fig. 8. Question is how best to combine a DEM with the mineral mapping product/s into a 2D or even a 3D thematic product.

Unlike traditional mapping techniques that rely on the subjective interpretation of non-mineral-specific information from remote sensing imagery like color aerial photography, this study shows how hyperspectral data can be processed to generate a more objective, accurate, reproducible thematic map of the regolith-geology that can be transferred as a method to other similar areas. However, this underlying methodology is also dependent on the user's ability to design a thematic model based on diagnostic mineral indicators. The diagnostic indicators in this study were: (i) serpentine, which is diagnostic of potential Ni-bearing peridotite, and its spatial proximity to (ii) abundant iron oxide, which is diagnostic of an overlying thick blanket of laterite rich where Ni was potentially concentrated (e.g. Fig. 9).

This study also exemplified the challenges in using airborne hyperspectral imagery for mineral exploration especially in more remote locations. That is, challenges related to survey logistics, cost, timeliness

and minimising the risk of cloud and vegetation cover and residual soil moisture after recent rainfall events, are all limiting factors. In future, many/most of these issues could be solved through access to imagery from upcoming hyperspectral satellite missions (Staenz et al., 2013), opening up new opportunities around rapid updating of areas that have been recently cleared by, for example, new roads and other infrastructure development, fires, landslides and tree fall exposing root systems after high wind events. Although the spatial resolution of hyperspectral satellite sensors is coarser than for airborne sensors (minimum 30 m), it corresponds to the smallest objects mapped on the field survey regolith-geology map used for comparison in this study (Fig. 3). Thus, as long as the spectral resolution is high enough (HSE Resurs-P, EnMAP, PRISMA, HISUI, ...), the methodology presented in this study could certainly bring the opportunity to have an updatable thematic regolith-geology map of New Caledonia based on periodic supply of hyperspectral satellite imaging of any newly exposed mineralogy.

## Acknowledgements

This study and the funding of Florian de Boissieu were supported by the National Centre for Technological Research “Nickel et son environnement” based in New Caledonia. Special thanks are also due to HyVista for acquisition and georeferencing the HyMap hyperspectral data.

## References

- Abedi, M., Norouzi, G.-H., Bahroudi, A., 2012. Support vector machine for multi-classification of mineral prospectivity areas. *Comput. Geosci.* 46, 272–283. <http://dx.doi.org/10.1016/j.cageo.2011.12.014>.
- Abrams, M., Tsu, H., Hulley, G., Iwao, K., Pieri, D., Cudahy, T., Kargel, J., 2015. The advanced spaceborne thermal emission and reflection radiometer (ASTER) after fifteen years: review of global products. *Int. J. Appl. Earth Obs. Geoinf.* 38, 292–301. <http://dx.doi.org/10.1016/j.jag.2015.01.013>.
- Anand, R.R., Paine, M., 2002. Regolith geology of the Yilgarn Craton, Western Australia: implications for exploration. *Aust. J. Earth Sci.* 49, 3–162. <http://dx.doi.org/10.1046/j.1440-0952.2002.00912.x>.
- Berk, A., Anderson, G.P., Acharya, P.K., Bernstein, L.S., Muratov, L., Lee, J., Fox, M.J., Adler-Golden, S.M., Chetwynd, J.H., Hoke, M.L., Lockwood, R.B., Gardner, J.A., Cooley, T.W., Borel, C.C., Lewis, P.E., Shettle, E.P., 2006. MODTRAN5: 2006 update. *Proceedings of SPIE*. SPIE 508–515. <http://dx.doi.org/10.1117/12.665077>.
- Boardman, J.W., Kruse, F.A., Green, R.O., 1995. Mapping target signatures via partial unmixing of Aviris data. In: *Summaries, Jet Propulsion Laboratory Publ. Presented at the Fifth JPL Airborne Earth Science Workshop*. Pasadena, California, USA. pp. 23–26.
- Camps-Valls, G., Bruzzone, L., 2005. Kernel-based methods for hyperspectral image classification. *IEEE Trans. Geosci. Remote Sens.* 43, 1351–1362. <http://dx.doi.org/10.1109/TGRS.2005.846154>.
- Chang, C.-C., Lin, C.-J., 2011. LIBSVM: a library for support vector machines. *ACM Trans. Intell. Syst. Technol.* 2, 27:1–27:27. <http://dx.doi.org/10.1145/1961189.1961199>.



- Clark, R.N., Roush, T.L., 1984. Reflectance spectroscopy: quantitative analysis techniques for remote sensing applications. *J. Geophys. Res.* 89, 12.
- Cocks, T., Jenssen, R., Stewart, A., Wilson, I., Shields, T., 1998. The HYMAP airborne hyperspectral sensor: the system, calibration, and performance. In: Presented at the First EARSeL Workshop on Imaging Spectroscopy. Zurich, Switzerland. pp. 37–42.
- Crowley, J.K., Brickey, D.W., Rowan, L.C., 1989. Airborne imaging spectrometer data of the Ruby Mountains, Montana: mineral discrimination using relative absorption band-depth images. *Remote Sens. Environ.* 29, 121–134. [http://dx.doi.org/10.1016/0034-4257\(89\)90021-7](http://dx.doi.org/10.1016/0034-4257(89)90021-7).
- Cudahy, T.J., Ramanaidou, E.R., 1997. Measurement of the hematite:goethite ratio using field visible and near-infrared reflectance spectrometry in channel iron deposits, Western Australia. *Aust. J. Earth Sci.* 44, 411–420. <http://dx.doi.org/10.1080/08120099708728322>.
- Cudahy, T.J., Hewson, R., Huntington, J.F., Quigley, M.A., Barry, P.S., 2001. The performance of the satellite-borne Hyperion hyperspectral VNIR-SWIR imaging system for mineral mapping at Mount Fitton, South Australia, in: *Geoscience and Remote Sensing Symposium*, 2001. IGARSS '01. IEEE 2001 International. Presented at the Geoscience and Remote Sensing Symposium, 2001. IGARSS '01. IEEE 2001 International, vol. 1, pp. 314–316. 10.1109/IGARSS.2001.976142.
- Cudahy, T., Jones, M., Thomas, M., Laukamp, C., Hewson, R., Rodger, A., Verrall, M., 2008. Next Generation Mineral Mapping: Queensland Airborne HyMap and Satellite ASTER Surveys 2006–2008 (CSIRO Report P2007/364).
- Cudahy, T.J., Hewson, R.D., Caccetta, M.S., Roache, A., Whitbourn, L.B., Connor, P., Coward, D.A., Mason, P., Yang, K., Huntington, J.F., Quigley, M., 2009. Drill core logging of plagioclase feldspar composition and other minerals associated with archaean gold mineralization at Kambalda, Western Australia, using a bidirectional thermal infrared reflectance system. *Rev. Econ. Geol.* 16, 223–235.
- Fauvel, M., Chanussot, J., Benediktsson, J.A., 2006. Evaluation of kernels for multiclass classification of hyperspectral remote sensing data. 2006 IEEE International Conference on Acoustics, Speech and Signal Processing, 2006. ICASSP 2006 Proceedings. Presented at the 2006 IEEE International Conference on Acoustics, Speech and Signal Processing, 2006. ICASSP 2006 Proceedings II. <http://dx.doi.org/10.1109/ICASSP.2006.1660467>.
- Green, R.O., Eastwood, M.L., Sarture, C.M., Chrien, T.G., Aronsson, M., Chippendale, B.J., Faust, J.A., Pavri, B.E., Chovit, C.J., Solis, M., Olah, M.R., Williams, O., 1998. Imaging spectroscopy and the airborne visible/infrared imaging spectrometer (AVIRIS). *Remote Sens. Environ.* 65, 227–248. [http://dx.doi.org/10.1016/S0034-4257\(98\)00064-9](http://dx.doi.org/10.1016/S0034-4257(98)00064-9).
- Huntington, J.F., Mauger, A.J., Skirrow, R.G., Bastrakov, E.N., Connor, P., Mason, P., Keeling, J.L., Coward, D.A., Berman, M., Phillips, R., Whitbourn, L.B., Heithersay, P.S., 2005. Automated mineralogical logging of core from the emmie bluff, iron oxide copper–gold prospect, South Australia. In: Presented at the PACRIM 2004, Aus IMM Publication Series. Adelaide South Australia. pp. 223–230.
- Kavitha, K., Arivazhagan, D.S., 2010. A novel feature derivation technique for SVM based hyper spectral image classification. *Int. J. Comput. Appl.* 1, 27–34. <http://dx.doi.org/10.5120/327-496>.
- King, T.V.V., Johnson, M.R., Hubbard, B.E., Drenth, B.J., 2011. Identification of mineral resources in Afghanistan—detecting and mapping resource anomalies in prioritized areas using geophysical and remote sensing (ASTER and HyMap) data (No. OFR-2011-1229). United States Geological Survey.
- Kokaly, R.F., Clark, R.N., 1999. Spectroscopic determination of leaf biochemistry using band-depth analysis of absorption features and stepwise multiple linear regression. *Remote Sens. Environ.* 67, 267–287. [http://dx.doi.org/10.1016/S0034-4257\(98\)00084-4](http://dx.doi.org/10.1016/S0034-4257(98)00084-4).
- Kruse, F.A., Boardman, J.W., Huntington, J.F., 2003. Comparison of airborne hyperspectral data and EO-1 hyperion for mineral mapping. *IEEE Trans. Geosci. Remote Sens.* 41, 1388–1400. <http://dx.doi.org/10.1109/TGRS.2003.812908>.
- Kruse, F.A., Perry, S.L., Caballero, A., 2006. District-level mineral survey using airborne hyperspectral data, Los Menudos, Argentina. *Ann. Geophys.* 49. <http://dx.doi.org/10.4401/ag-3154>.
- Launer, P.J., 1952. Regularities in the infrared absorption spectra of silicate minerals. *Am. Mineral.* 37, 764–784.
- Logan, L.M., Hunt, G.R., Salisbury, J.W., Balsamo, S.R., 1973. Compositional implications of Christiansen frequency maximums for infrared remote sensing applications. *J. Geophys. Res.* 78, 4983–5003. <http://dx.doi.org/10.1029/JB078i023p04983>.
- Lyon, R.J.P., Burns, E.A., 1963. Analysis of rocks and minerals by reflected infrared radiation. *Econ. Geol.* 58, 274–284. <http://dx.doi.org/10.2113/gsecongeo.58.2.274>.
- Lyon, R.J.P., 1965. Analysis of rocks by spectral infrared emission (8–25 microns). *Econ. Geol.* 60, 715–736. <http://dx.doi.org/10.2113/gsecongeo.60.4.715>.
- Mudd, G.M., Jowitt, S.M., 2014. A detailed assessment of global nickel resource trends and endowments. *Econ. Geol.* 109, 1813–1841. <http://dx.doi.org/10.2113/econgeo.109.7.1813>.
- Nahon, D., 2003. Altérations dans la zone tropicale. Signification à travers les mécanismes anciens et/ou encore actuels. *C.R. Geosci.* 335, 1109–1119. <http://dx.doi.org/10.1016/j.crte.2003.10.008>.
- Rodger, A., 2011. SODA: a new method of in-scene atmospheric water vapor estimation and post-flight spectral recalibration for hyperspectral sensors application to the HyMap sensor at two locations. *Remote Sens. Environ.* 115, 536–547. <http://dx.doi.org/10.1016/j.rse.2010.09.022>.
- Rowan, L.C., Simpson, C.J., Mars, J.C., 2004. Hyperspectral analysis of the ultramafic complex and adjacent lithologies at Mordor, NT, Australia. *Remote Sens. Environ.* 91, 419–431. <http://dx.doi.org/10.1016/j.rse.2004.04.007>.
- Sabins, F.F., 1999. Remote sensing for mineral exploration. *Ore Geol. Rev.* 14, 157–183. [http://dx.doi.org/10.1016/S0169-1368\(99\)00007-4](http://dx.doi.org/10.1016/S0169-1368(99)00007-4).
- Salisbury, J.W., Walter, L.S., 1989. Thermal infrared (2.5–13.5 (m) spectroscopic remote sensing of igneous rock types on particulate planetary surfaces. *J. Geophys. Res.* 94, 9192–9202. <http://dx.doi.org/10.1029/JB094iB07p09192>.
- Sevin, B., 2014. Cartographie du Régolithe sur Formation Ultrabasique de Nouvelle-Calédonie: Localisation dans l'espace et le temps des gisements nickélfères. UNC, Noumea.
- Sonntag, I., Laukamp, C., Hagemann, S.G., 2012. Low potassium hydrothermal alteration in low sulfidation epithermal systems as detected by IRS and XRD: An example from the Co–O mine, Eastern Mindanao, Philippines. *Ore Geology Reviews, Primary Geochemical Characteristics of Mineral Deposits: Implications for Exploration* 45, 47–60. <http://10.1016/j.oregeorev.2011.08.001> (<http://dx.doi.org/10.1016/j.oregeorev.2011.08.001>).
- Staenz, K., Mueller, A., Heiden, U., 2013. Overview of terrestrial imaging spectroscopy missions, in: *Geoscience and Remote Sensing Symposium (IGARSS)*, 2013 IEEE International. Presented at the Geoscience and Remote Sensing Symposium (IGARSS), 2013 IEEE International, pp. 3502–3505. 10.1109/IGARSS.2013.6723584.
- Sunshine, J.M., Pieters, C.M., Pratt, S.F., 1990. Deconvolution of mineral absorption bands: an improved approach. *J. Geophys. Res.* 95, 6955–6966. <http://dx.doi.org/10.1029/JB095iB05p06955>.
- Vapnik, V.N., 1998. *Statistical Learning Theory*. Wiley.
- van der Meer, F.D., van der Werff, H.M.A., van Ruitenbeek, F.J.A., Hecker, C.A., Bakker, W.H., Nooten, M.F., van der Meijde, M., Carranza, E.J.M., de Smeth, J.B., Woldai, T., 2012. Multi- and hyperspectral geologic remote sensing: a review. *Int. J. Appl. Earth Obs. Geoinf.* 14, 112–128. <http://dx.doi.org/10.1016/j.jag.2011.08.002>.
- van der Meer, F.D., 1995. Estimating and simulating the degree of serpentinization of peridotites using hyperspectral remotely sensed imagery. *Nat. Resour. Res.* 4, 84–98. <http://dx.doi.org/10.1007/BF02257019>.
- van der Meer, F.D., 2000. Spectral curve shape matching with a continuum removed CCSSM algorithm. *Int. J. Remote Sens.* 21, 3179–3185. <http://dx.doi.org/10.1080/01431160050145063>.